Nucleic Acids Research, 2003, Vol. 31, No. 10 ***2671–2682***
DOI: 10.1093/nar/gkg350

A crystallographic study of the binding of 13 metal ions to two related RNA duplexes

Eric Ennifar, Philippe Walter and Philippe Dumas*

Institut de Biologie Moléculaire et Cellulaire, CNRS-UPR 9002, 15 rue René Descartes, 67084 Strasbourg cedex, France

Received January 7, 2003; Revised February 27, 2003; Accepted March 13, 2003

ABSTRACT

Metal ions, and magnesium in particular, are known to be involved in RNA folding by stabilizing secondary and tertiary structures, and, as cofactors, in RNA enzymatic activity. We have conducted a systematic crystallographic analysis of cation binding to the duplex form of the HIV-1 RNA dimerization initiation site for the subtype-A and -B natural sequences. Eleven ions (K^+, Pb^{2+}, Mn^{2+}, Ba^{2+}, Ca^{2+}, Cd^{2+}, Sr^{2+}, Zn^{2+}, Co^{2+}, Au^{3+} and Pt^{4+}) and two hexammines $[Co(NH_3)_6]^{3+}$ and $[Ru(NH_3)_6]^{3+}$ were found to bind to the DIS duplex structure. Although the two sequences are very similar, strong differences were found in their cation binding properties. Divalent cations bind almost exclusively, as Mg^{2+}, at 'Hoogsteen' sites of guanine residues, with a cation-dependent affinity for each site. Notably, a given cation can have very different affinities for a priori equivalent sites within the same molecule. Surprisingly, none of the two hexammines used were able to efficiently replace hexahydrated magnesium. Instead, $[Co(NH_3)_4]^{3+}$ was seen bound by inner-sphere coordination to the RNA. This raises some questions about the practical use of $[Co(NH_3)_6]^{3+}$ as a $[Mg(H_2O)_6]^{2+}$ mimetic. Also very unexpected was the binding of the small Au^{3+} cation exactly between the Watson–Crick sites of a G-C base pair after an obligatory deprotonation of N1 of the guanine base. This extensive study of metal ion binding using X-ray crystallography significantly enriches our knowledge on the binding of middle-weight or heavy metal ions to RNA, particularly compared with magnesium.

INTRODUCTION

Metal cations, and especially divalent cations, often play a key role for RNA folding being involved in the stability of structural motifs. In addition, they have been shown to be directly implicated (but not always) in ribozyme reactions. Investigations about metal ion binding have become widespread with the growing interest for RNA in structural biology and the increasing number of RNA structures solved. Biochemical methods may allow precise identification of metal ion binding sites within RNA (1–3), for instance by using chemical probing combined with interference experiments and site-directed mutagenesis. Nuclear Magnetic Resonance (NMR) spectroscopy can also provide a dynamic view of ion–RNA interactions in solution, provided an isotope of the considered ion exists with a suitable nuclear spin number (4–9). Electron Paramagnetic Resonance spectroscopy is useful to probe the environment of a metal, but is also limited to spectroscopically active species like Co(II) or Mn(II), but not Zn(II), Ca(II) or Mg(II) (10). Brownian-dynamics simulations have also been proposed to explore metal ion binding of NMR structures (11). Doubtless, X-ray crystallography is the most powerful method for the localization of metal ions. Practically, information obtained in such a way (for RNA as well as for proteins) has often been a by-product of soaking of the crystals into various heavy atom salts in view of solving the structure by either the Multiple Isomorphous Replacement or the Multiple Anomalous Dispersion (MAD) method. Quite often, however, the chemical information is shadowed by the technical problem or by interest in the newly determined structure, and is not given due interest. In the present case, results obtained in such a way (as for lead and ruthenium derivatives) were systematically analysed and, in addition, a study was performed for its own chemical interest. Crystallographically, the accuracy of the resulting information depends on the number of electrons of the considered cation and on the quality of the crystals used for data collection. Importantly, atoms with a sufficient number of electrons often have a significant 'anomalous dispersion' at the wavelength used for data collection. This means that the inner electrons, being tightly bound to the nucleus, respond significantly out of phase of the X-ray excitation. This has the interesting consequence of providing an 'anomalous signature' to such atoms allowing their unambiguous localization and identification in so-called 'anomalous difference maps' (see Materials and Methods for more details). As powerful the crystallographic technique can be, it should be kept in mind that it relies on data obtained from densely packed molecules that obviously cannot be viewed as isolated. It is likely that oddities reported from this work (e.g. the different affinities of a given cation for a priori equivalent sites) are related to this fact, although certainly not in a straightforward way. Another (often neglected) source of problems related to the crystalline state stems from ion concentrations in crystallization drops

*To whom correspondence should be addressed. Tel: +33 388 41 7002; Fax: +33 388 6022 18; Email: p.dumas@ibmc.u-strasbg.fr

being potentially different from their concentrations in solvent channels, particularly within a crystal made of charged molecules.

We have used for the present study two natural sequences of a 23-nt fragment of the HIV-1 RNA genome. This fragment corresponds to the RNA dimerization initiation site (DIS) and the two sequences are representative of the most widespread HIV-1 subtypes (subtypes-A and -B). The DIS allows homodimerization of the RNA by the formation of a loop–loop complex, or 'kissing-complex', thanks to a self-complementary sequence within the loop (12). Alternatively, it allows the formation of an 'extended duplex' (Fig. 1a). *In vitro*, the respective amount of each form depends a priori on the folding conditions and it has been shown that the basic nucleocapsid protein promotes the formation of the duplex form (13). *In vivo*, it is supposed that there is stabilization of the initial 'kissing-complex' into the duplex form. We have previously solved the crystal structures of the DIS loop–loop form for subtypes-A and -B (14), and the extended duplex form for subtype-A (15) (Fig. 1b) and subtype-B (E.Ennifar *et al.*, manuscript in preparation). The two sequences are very similar (Fig. 1a) and crystals of the duplex form for each sequence were obtained under very similar low-salt crystallization conditions. In spite of this, the two structures revealed quite a different magnesium binding pattern: as many as eight specific Mg^{2+} binding sites were found in the subtype-A DIS duplex (15) (Fig. 1b), whereas none were found in the subtype-B DIS duplex (apart for weak sites involved in packing interactions). Here, we compare in detail the respective metal ion binding properties of both structures, whereas the detailed description of the subtype-B duplex, which revealed an unexpected metal ion-dependent self-cleaving activity, will be described elsewhere (E.Ennifar *et al.*, manuscript in preparation). Among all tested cations, 11 were found to bind the subtype-A DIS duplex (Pb^{2+}, Mn^{2+}, Ba^{2+}, Ca^{2+}, Cd^{2+}, Sr^{2+}, Zn^{2+}, Co^{2+} and Pt^{4+} and the two hexammines $[Co(NH_3)_6]^{3+}$ and $[Ru(NH_3)_6]^{3+}$, and seven to the subtype-B DIS duplex (K^+, Mn^{2+}, Ba^{2+}, Zn^{2+}, Co^{2+}, Au^{3+} and Pt^{4+} as well as $[Ru(NH_3)_6]^{3+}$).

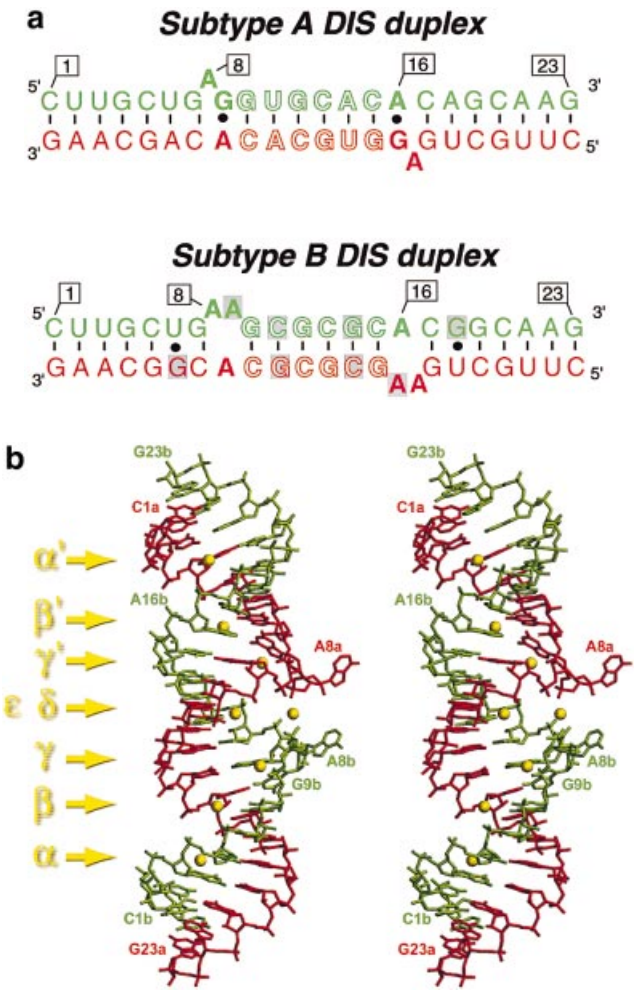

Figure 1. Structures of the oligonucleotides used in this study. The two homologous strands are represented in red and green. (**a**) Primary and secondary structure of subtype-A and -B DIS duplex. The changes in sequence are highlighted in grey in the subtype-B duplex. (**b**) Stereoview showing the crystal structure of the trigonal form of the subtype-A DIS duplex (15) with magnesium cations represented as yellow spheres and labeled with Greek letters.

MATERIALS AND METHODS

RNA synthesis, purification and crystallization

A chemically synthesized 23mer RNA was purchased from Dharmacon Research and purified using an ion-exchange Nucleopac PA-100 (Dionex) column as described (15). RNA at a concentration of 60 µM was annealed for 3 min in water at 90°C, cooled to room temperature and incubated for 1 h at 37°C in a crystallization buffer (subtype-A DIS: 20 mM Na cacodylate pH 7.0, 5 mM $MgCl_2$, 150 mM KCl; subtype-B DIS: 20 mM Na cacodylate pH 7.0, 5 mM $MgCl_2$, 300 mM KCl). Samples were then concentrated to ~600 µM and crystallization was performed in sitting drop by mixing 9 µl of concentrated RNA with 0.9 µl of precipitant (50 mM spermine and 10% methylpentanediol (MPD) for the subtype-A DIS, 50 mM spermine and 20–30% MPD for the subtype-B DIS). Drops were equilibrated at 37°C with a 500 µl reservoir made with 50% MPD, 50 mM Na cacodylate, 100 mM $MgCl_2$ and 300 mM KCl. Crystals appeared within 1–2 weeks and were stabilized by slowly adding reservoir solution, and cooled to room temperature.

Soaking of crystals and data collection

Soaking of crystals was achieved by using reservoir solutions supplemented with the desired salt. This also allowed stabilization and cryoprotection of the crystals. In some cases, magnesium was removed, or its concentration reduced, to avoid competition with the tested cation (see Table 1 for the concentrations of each cation and of magnesium). Soaking time was comprised indifferently between 2 days and a week apart for zinc, ruthenium, platinum and lead (see Table 1). Potassium chloride and sodium cacodylate buffer were kept at 300 and 50 mM, respectively. Cobalt hexammine was present initially at 2 mM concentration in the solution prepared for soaking, but crystals appeared rapidly at room temperature (apparently due to the large concentration of MPD). As a consequence, the exact concentration of cobalt hexammine used for soaking is not known. In aqueous solution, ruthenium hexammine is known to be unstable and to be oxidized into the

Table 1. Experimental data

Salts[a]	Max. Res.	Unit cell (Å)	R_{sym}[b] (%)	Completeness[b] (%)	Redund.	I/σ[b]	f'' (ē)	X-ray[c]
Subtype-A DIS duplex (Space group $P3_121$)								
Native (PDB id: 462D)	2.1 Å	a = b = 59.02, c = 63.98	6.0 (21.3)	99.9 (99.1)	9.2	31.8 (6.8)	–	ID14-1
$MnCl_2$ 100 mM ($MgCl_2$ 0 mM)	3.1 Å	a = b = 59.07, c = 63.64	4.2 (10.4)	91.5 (82.1)	1.5	15.7 (7.00)	2.8	Rot. anode
$CoCl_2$ 100 mM ($MgCl_2$ 0 mM)	2.9 Å	a = b = 59.17, c = 64.00	6.6 (13.9)	99.1 (94.1)	3.9	20.4 (8.6)	3.6	Rot. anode
$SrCl_2$ 100 mM ($MgCl_2$ 0 mM)	2.8 Å	a = b = 57.88, c = 65.80	5.4 (20.4)	99.3 (98.2)	6.5	33.7 (8.9)	1.8	Rot. anode
$ZnCl_2$ 100 mM ($MgCl_2$ 0 mM), 1 month	1.9 Å	a = b = 59.35, c = 63.71	4.0 (19.5)	95.2 (69.3)	3.0	26.6 (2.8)	3.9	BW7A
$CaCl_2$ 100 mM[d] ($MgCl_2$ 0 mM)	2.7 Å	a = b = 57.91, c = 65.165	4.9 (29.3)	99.6 (99.7)	7.4	24.1 (5.7)	1.3	DW32
$CdCl_2$ 15 mM ($MgCl_2$ 5 mM)	2.9 Å	a = b = 58.98, c = 64.99	4.4 (22.0)	99.1 (98.2)	4.0	22.3 (6.1)	4.6	Rot. anode
$BaCl_2$ 50 mM ($MgCl_2$ 0 mM)	2.8 Å	a = b = 58.01, c = 65.42	7.9 (28.6)	98.6 (99.0)	4.9	20.8 (5.1)	8.4	Rot. anode
$PtCl_4$ 1 mM ($MgCl_2$ 5 mM), 3–5 h	2.9 Å	a = b = 58.91, c = 65.19	4.3 (15.9)	99.9 (99.9)	4.6	23.8 (8.8)	6.9	Rot. anode
Pb acetate[d,e] ($MgCl_2$ 100 mM), 12 h	2.8 Å	a = b = 59.20, c = 65.80	4.5 (29.9)	96.3 (94.5)	na	12.6 (3.2)	8.5	Rot. anode
$[Ru(NH_3)_6]Cl_3$ 12 mM ($MgCl_2$ 100 mM), 2–3 days	2.6 Å	a = b = 59.11, c = 64.15	3.7 (9.8)	98.5 (93.1)	4.4	40.3 (15.1)	3.3	Rot. anode
$[Co(NH_3)_6]Cl_3$[e] ($MgCl_2$ 0 mM)	2.5 Å	a = b = 58.80, c = 65.10	6.1 (36.6)	97.8 (96.4)	6.2	30.4 (4.6)	4.6	Rot. anode
Subtype-B DIS duplex (Space group $P2_12_12$)								
Native (PDB id: 1M28)	1.6 Å	a = 43.98, b = 47.53, c = 57.66	6.3 (24.0)	99.5 (99.0)	9.2	23.8 (10.0)	–	ID14-2
$MnCl_2$ 100 mM ($MgCl_2$ 0 mM)	2.6 Å	a = 42.54, b = 47.83, c = 58.68	6.0 (8.3)	98.4 (92.7)	3.3	21.1 (12.0)	2.4	BM30
$CoCl_2$ 100 mM ($MgCl_2$ 0 mM)	2.5 Å	a = 43.70, b = 47.55, c = 57.77	6.6 (23.2)	96.1 (96.0)	2.7	12.0 (3.7)	3.6	Rot. anode
$ZnCl_2$ 100 mM ($MgCl_2$ 0 mM), 1 month	1.9 Å	a = 43.79, b = 47.63, c = 58.00	6.8 (8.5)	87.0 (41.9)	4.8	19.7 (10.1)	7.4	BM30
$BaCl_2$ 100 mM ($MgCl_2$ 0 mM)	2.6 Å	a = 43.45, b = 47.45, c = 57.93	6.5 (13.2)	99.2 (94.5)	5.6	27.5 (12.4)	3.9	Rot. anode
$[Ru(NH_3)_6]Cl_3$ 12 mM ($MgCl_2$ 100 mM), 2–3 days	2.0 Å	a = 43.77, b = 47.87, c = 57.26	3.9 (11.2)	99.1 (99.3)	6.1	41.8 (11.2)	1.3	BM30
$AuCl_3$ 10 mM ($MgCl_2$ 100 mM)	2.3 Å	a = 43.56, b = 47.46, c = 57.96	4.3 (10.1)	99.7 (99.9)	6.8	43.1 (10.8)	10.5	BM30
$PtCl_4$ 1 mM ($MgCl_2$ 5 mM), 3–5 h	2.5 Å	a = 44.08, b = 47.59, c = 57.63	4.1 (12.8)	68.9 (71.9)	3.5	24.7 (5.1)	10.9	BM30

[a]Unless specifically indicated in this column, soaking time was comprised between 2 days and 1 week. PDB id codes for subtype-A duplex with Zn^{2+} (1NLC), with ruthenium hexammine (1NLE); for subtype-B duplex with Mn^{2+} (1M29).
[b]The values in parentheses correspond to the higher-resolution shell.
[c]Different beam lines used: ID14-1,2 and BM30 (ESRF, Grenoble), BW7A (DESY, Hamburg), DW32 (LURE, Orsay).
[d]Data were processed by averaging the intensities of Bijvoet pairs.
[e]Salt concentration in crystallization drops was saturating.

trinuclear compound 'ruthenium red' $[Ru(NH_3)_5$-*O*-$Ru(NH_3)_4$-*O*-$Ru(NH_3)_5]Cl_6$ within 2 weeks. Therefore, fresh solutions were used for soaking. Since no trinuclear compound was detected in electron density maps, it can be concluded that ruthenium hexammine was bound. Apart for the lead-soaked crystal that was used at room temperature for data collection (prior establishment of the following freezing conditions), all crystals were flash-frozen into liquid ethane and kept under a nitrogen gas stream (Oxford Cryosystems) at 110 K during data collection. Data were collected on our laboratory rotating anode or on various synchrotron X-ray sources (Table 1); they were processed with the HKL package (16). All structures were refined with CNS (17). Native structures were refined at 2.1 Å resolution (R = 21.7%, R_{free} = 21.9%) for the subtype-A DIS, and at 1.6 Å resolution (R = 24.2%, R_{free} = 25.0%) for the subtype-B DIS.

Localization of metal ions

The identity of metal ions with sufficient anomalous scattering, i.e. with suitable f'' value (see Table 1), was confirmed by calculating anomalous difference maps with the CCP4 suite (18). Such maps are calculated with coefficients $(F_{obs}^{+} - F_{obs}^{-})$ $e^{i(\varphi+\pi/2)}$, where φ is the phase of the refined model and F_{obs}^{+} and F_{obs}^{-} the experimental amplitudes corresponding to a 'Bijvoet pair' of reflections (apart for experimental errors, F_{obs}^{+} and F_{obs}^{-} are equal in the absence of anomalous dispersion, which results in a noisy and featureless anomalous difference map). Anomalous difference maps were calculated in various resolution ranges depending on each dataset. In the case of strontium- and especially calcium-bound structures, the anomalous signal was too weak due to relatively low resolution of the collected data, and to low occupancy and high thermal agitation (or static disorder) of these ions. Strontium ions could easily be localized on usual difference maps with coefficients $(F_{obs} - F_{calc})$, but Ca^{2+} ions remained difficult to localize accurately. Binding sites for this ion, however, seem to match those of strontium. Lead ions were also localized by usual $(F_{obs} - F_{calc})$ difference map due to the lack of experimental anomalous differences resulting from low redundancy and rather poor quality of the data that were collected at room temperature on a laboratory rotating anode. Their localization, however, was unambiguous due to the large *Z*-value of lead. A particular mention should be made of potassium since, despite a rather low f'' value (0.42 e^- at λ = 0.93 Å), its binding was convincingly confirmed in anomalous difference maps. This is a valuable alternative to

its replacement with other cations like thallium (19,20), since no additional experiment is required and, most importantly also, because it does not rely on the optimistic assumption that another cation will indeed substitute for potassium.

No metal ion binding was observed in subtype-A DIS after soaking of the crystals in RbCl, $Rh(NH_3)_5Cl_3$, $RhCl_3$, $InCl_3$, CsCl, $IrCl_4$, $AuCl_3$, $HgCl_2$, Hg acetate, $SmCl_3$, $EuNO_3$ and $TbCl_3$, and in subtype-B DIS after soaking of the crystals in RbCl, $RhCl_3$, $InCl_3$ and $HgCl_2$. (Note that although many trials were performed, subtype-A and -B crystals were not systematically submitted to identical soaking experiments. This is only due to the practical difficulty of performing truly exhaustive experiments in a reasonable time.)

Lead-induced cleavage

Crystals of the subtype-A DIS RNA duplex (trigonal form) were washed into stabilizing solution and dissolved into an acetate buffer solution (2 mM Mg acetate, 20 mM Na cacodylate pH 7.0, 25 mM KCl). For comparison with lead-cleavage of the kissing-loop form, an RNA sample at 6 μM in water was heat-denatured at 90°C for 5 min and then immediately cooled on ice for 5 min. Acetate buffer solution was then added to yield a sample of the kissing-loop form. Both these kissing-loop and duplex samples were then incubated for 90 min either in presence of 11 mM lead acetate or in water (for negative control) at 20°C. Such a low temperature was chosen to avoid any potential kissing-loop complex/duplex transition or too important conformational change due to thermal motion. Lead cutting was stopped by addition of EDTA (29 mM final concentration). Samples were analyzed by a denaturing 15% polyacrylamide gel electrophoresis.

RESULTS AND DISCUSSION

Mn^{2+}, Co^{2+} and Zn^{2+} are the best Mg^{2+} mimetics

Despite similar sequences and almost identical crystallization conditions, subtype-A and -B DIS duplex crystal structures display a very different magnesium binding pattern: eight rather strong magnesium sites were localized in the subtype-A DIS duplex (Fig. 1b) (15), whereas only two partially occupied magnesium sites could be localized in the subtype-B DIS duplex. A comparison between monoclinic and trigonal crystal forms of the subtype-A DIS duplex (obtained under identical crystallization conditions) showed that the two forms share exactly the same magnesium sites (15), indicating that magnesium binding is not significantly affected by crystal packing in this structure. It is therefore quite surprising to observe such a disparity in magnesium binding between subtype-A and -B DIS duplexes having very similar stem sequences.

The subtype-A DIS duplex structure is not affected by the replacement of Mg^{2+} either by Zn^{2+}, Mn^{2+} or Co^{2+}: all the structures obtained in presence of these cations are perfectly isomorphous with the native one. These three divalent ions share very similar RNA binding properties and essentially bind to the same sites as Mg^{2+}, i.e. in the major groove, on Hoogsteen sites (N7 and O6 atoms) of guanines. Binding occurs either by outer-sphere interactions via water molecules as illustrated by Zn^{2+} replacing Mg^{2+} at site β (Figs 2 and 3a), or by inner-sphere interactions around bulged-out adenines (Fig. 2). However, some differences in relative affinities compared with magnesium are observed: Mg sites α', β and especially γ and γ', are by far favourite binding sites for these three divalent ions, whereas Mg sites α, δ, ε and β are not, or only poorly replaced, depending on each of them (Fig. 2). Clearly, this similarity with magnesium binding is due to identical octahedral coordination, similar ionic radii and ion-ligand distance (Table 2). By its ability to replace magnesium, and a significant anomalous scattering, we have recently shown that zinc may be particularly efficient for X-ray structure determination of RNA using MAD technique (21).

The situation is different for the subtype-B DIS duplex. In that structure, a unique and very strong binding site was found for Zn^{2+}, Mn^{2+} and Co^{2+} (Fig. 2). This site involves a direct interaction with a negatively charged pocket formed by two phosphates and N7 atom of a guanosine. This pocket results from a local conformational change at the A9-G10 step (Fig. 3b) induced only upon binding of these three cations since it was not observed in the presence of magnesium in the native structure. It is thus remarkable that these three cations can replace perfectly well Mg^{2+} in the subtype-A structure, whereas they occupy a specific site not occupied by Mg^{2+} in the subtype-B structure. Notably also, despite an almost perfect 2-fold non-crystallographic axis relating two potential binding sites, only the one shown in Figure 3b is occupied with Zn^{2+} and Mn^{2+}, whereas both sites are occupied in presence of Co^{2+} (Fig. 2). It is thus interesting to note that the binding of cations to seemingly identical RNA sites depends on subtle changes that are not immediately rationalized. The same remark will be made in other cases. It may be thought that such different affinities result from differences in the hydration pattern [comprising the 'delocalized' ions that are important in the overall energetic balance (22)]. One can easily imagine that the differences in hydration result themselves from subtle differences in the local environment in the crystal. Figure 3a, for example, illustrates the existence of a precise network of water molecules around a Zn^{2+} cation that could depend on medium-range interactions existing in a crystal. This is in agreement with the now common description of water as an integral part of nucleic acid structure (23,24). It is thus likely that these non-equivalent sites in the crystal are indeed equivalent in solution (i.e. that Zn^{2+}, Mn^{2+} and Co^{2+} bind equally on both of them).

Cobalt(III) and ruthenium(III) hexammine do not replace hexahydrated Mg^{2+}

Ruthenium(III) hexammine was used as heavy atom for solving the structure of both subtype-A and -B DIS crystals. Due to very good isomorphism with the native structure and high substitution, this heavy-atom derivative provided very good phase information. Although iridium or osmium hexammine can provide a larger isomorphous signal (by their higher *Z*-value) and are also more suitable for MAD experiments (25–28), ruthenium hexammine has the advantage of being commercially available since it is widely used in its oxidized form for electron microscopy studies.

In subtype-A DIS crystals stabilized in a solution containing 100 mM Mg^{2+} and 10 mM ruthenium hexammine, the ruthenium cation displaced $[Mg(H_2O)_6]^{2+}$ cations involved in weak packing interactions, but did not replace any

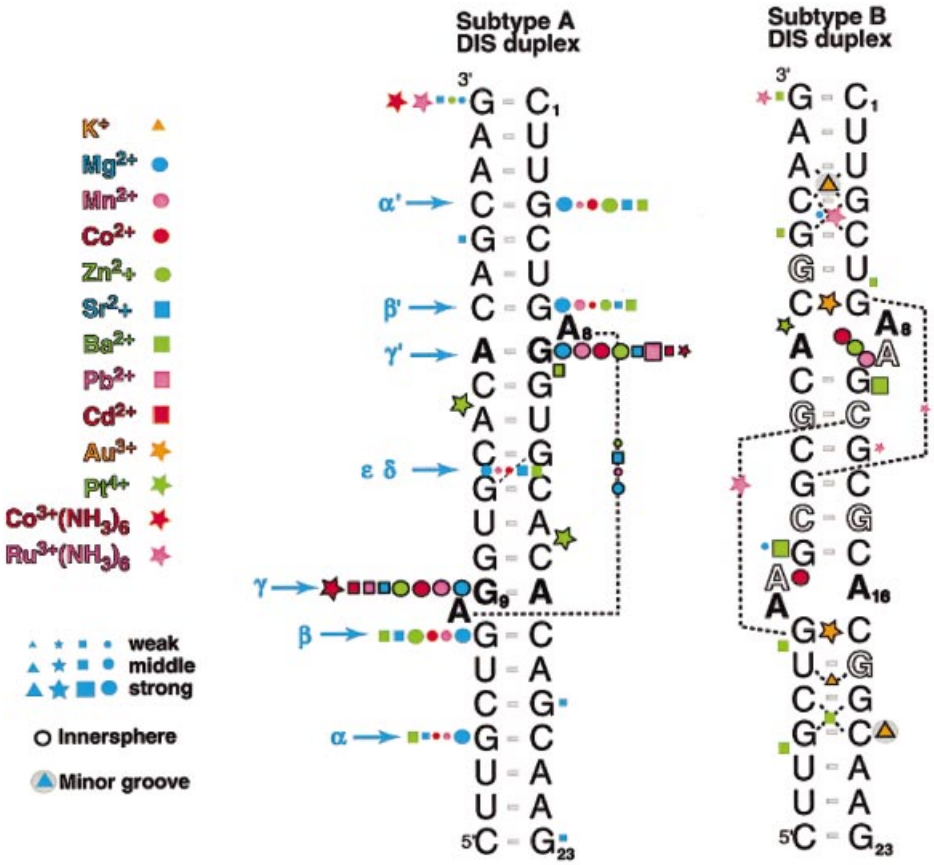

Figure 2. Schematic drawing summarizing cation binding to subtype-A and -B DIS duplexes. The nature of each cation is represented by a geometric symbol (square, circle, star or triangle) and a colour. The size of the symbol depicts the binding strength (weak, average or strong). Unless otherwise stated, the binding sites lie within the major groove of duplexes and involve outer-sphere contacts.

hexahydrated magnesium inside the DIS duplex (Fig. 2). Notably, it did not replace magnesium ε located on the symmetry axis of the two adjacent GC base pairs in the sequence 5′-UGCA-3′ (this is mentioned in view of a forthcoming discussion). This magnesium was present in both the subtype-A duplex and kissing-loop complex (14,15). Decreasing Mg^{2+} concentration in crystallization drops from 100 to 2 mM did not improve ruthenium hexammine binding to the structure, which shows that it did not compete with magnesium, at least in this concentration range. The strongest ruthenium hexammine binding site corresponds to a weak hexahydrated magnesium cation binding site in the native structure and is close to the interface of two stacked duplexes forming infinite helices. The binding is on N7 and O6 of G23 with an electrostatic interaction with the phosphates of A22 and G23 (Fig. S1a in Supplementary Material). Such binding was already observed for iridium and rhodium hexammine in a small RNA duplex with mismatches (27,28), without magnesium cation in the native structure.

For the subtype-B DIS duplex, the situation was quite different since magnesium could be completely replaced in crystallization drops by 25 mM ruthenium hexammine without inducing any significant structural distortion. This is in full agreement with the lack of ordered Mg^{2+} cations in the native structure. In such conditions, five ruthenium hexammine binding sites were localized and used for structure determination (Fig. 2). For two of them, the hexammine directly bridges two phosphates across the major groove (Ru1 in Fig. S1b in Supplementary Material). This kind of binding was already observed in A-form nucleic acid duplexes for hexahydrated Mg^{2+} cations (29,30). In the present structure, the binding is stabilized by additional interactions with phosphate groups from symmetry-related duplexes (Fig. S1b). As revealed by inspection of residual electron density maps in native structures, hexahydrated magnesium might also bind analogously, but weakly, in both subtype-A and -B DIS duplex crystals. For the three other sites, the ruthenium hexammine is bound inside the major groove and interacts with the Hoogsteen site of guanines. In the case illustrated by Figure S1c, the cation is centrally located on the local symmetry axis of the two adjacent G-C base pairs embedded in the short helix formed by 5′-UGCU-3′ and 5′-GGCA-3′. This site is therefore somewhat comparable to the hexahydrated magnesium binding site ε (corresponding to the self-complementary sequence 5′-UGCA-3′) in both subtype-A duplex and kissing-loop complexes (see above). This emphasizes the importance of 'details' in the shaping of a cation binding site since, even though the two sites are comparable, $[Mg(H_2O)_6]^{2+}$ is unable to bind where $[Ru(NH_3)_6]^{3+}$ binds, and vice versa. Also, as already mentioned

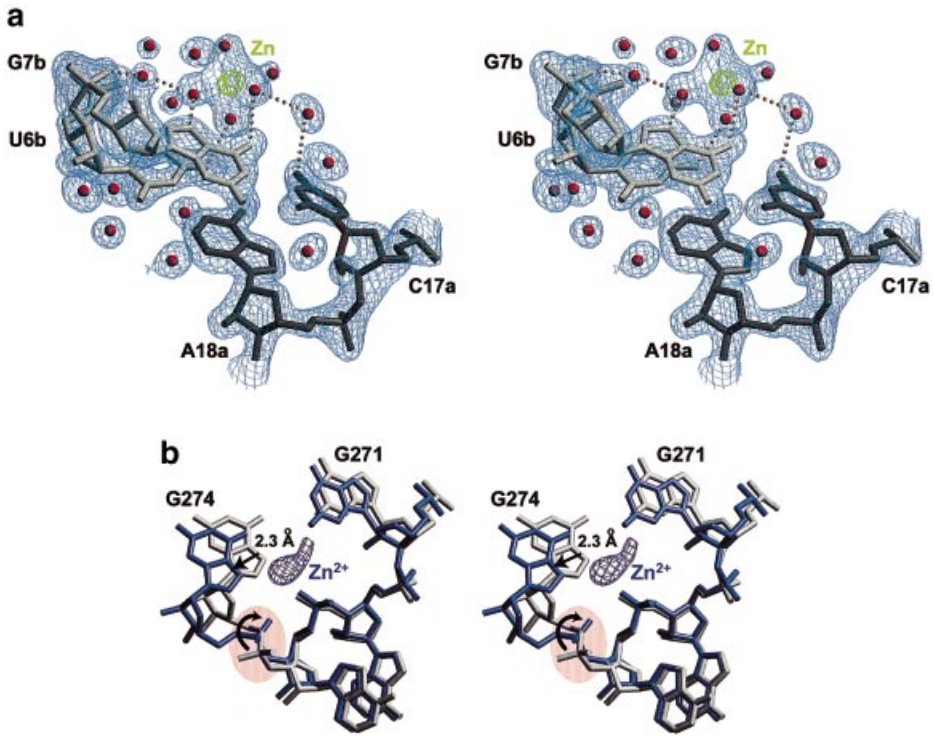

Figure 3. (**a**) Stereoview of Mg^{2+}-like hexahydrated Zn^{2+} binding to the Hoogsteen site of a guanine base (site β in Fig. 1a). The electron density map (in blue) was calculated with ($2F_{obs} - F_{calc}$) coefficients and contoured at 1.2 σ above mean level. The green peak corresponds to an anomalous difference map contoured at 10 σ above mean level. The picture, to be compared with figure 5 in Ennifar *et al*. (15), illustrates very well the involvement of a network of water molecules in cation binding. (**b**) Stereoview showing the conformational change induced upon Zn^{2+} binding in the bulge region of the subtype-B DIS duplex. The native structure is depicted in gray and the Zn-bound structure in purple. The anomalous map contoured at 8 σ above mean level clearly shows a delocalization of the divalent cation.

Table 2. Some physico-chemical features of the cations used in this study (from www.webelements.com)

Cation	Distance ion – O (Å)	Ionic radius (Å)	Preferred coordination	pK_a
K^+	2.80	1.41	4, 6, 8	
Mg^{2+}	2.09	0.86	6	11.4
Mn^{2+}	2.19	0.81	6	10.6
Co^{2+}	2.11	0.79	6	10.2
Co^{3+}		0.68	6	
Zn^{2+}	2.10	0.88	4, 6	9.0
Sr^{2+}	2.64	1.32	8	
Ca^{2+}	2.42	1.14	6, 8	12.9
Ba^{2+}	2.80	1.49	8	13.5
Cd^{2+}	2.30	1.09	4, 6	9.6
Pb^{2+}		1.33	6	7.7
Pt^{4+}		0.71	8	
Au^{3+}		0.82	4	
Ru3+		0.82	6	

for other cations, there is no ruthenium bound at the a priori equivalent site related by non-crystallographic symmetry in the subtype-B duplex.

Cobalt(III) hexammine is commonly used as a probe replacing hexahydrated magnesium in NMR studies (4–8) or in biochemical experiments (31). This is based upon the very low exchanging rate of ammines in such complex (32). It is also frequently used as a counter ion in the crystallization process of nucleic acids structures, and observed at potential $[Mg\ (H_2O)_6]^{2+}$ sites in resulting structures (33,34). In the present study, subtype-A DIS crystals were soaked in a magnesium-free solution saturated with cobalt hexammine (see Materials and Methods). One binding site for cobalt hexammine was found identical to the major ruthenium hexammine binding site, at the interface between two stacked helices (Fig. 2). This was not unexpected. On the contrary, very unexpected were the following observations in complete contradiction to the common use of cobalt hexammine as a perfect mimic for hexahydrated magnesium. First, anomalous difference maps unambiguously showed two cobalt cations bound at the two positions γ and γ' for partially dehydrated Mg^{2+} cation, without inducing any local distortion in comparison of the Mg^{2+}-bound structure (Figs 2 and 4). This is surprising since such a binding requires the loss of two ammines for a direct interaction between the cation and a pro(R) phosphate oxygen and N7 of a guanine base. Similar binding was already observed on a DNA X-ray structure (35). Secondly, as in the case of ruthenium hexammine, none of the five strongest hexahydrated magnesium binding sites inside the duplex structure was replaced by cobalt hexammine. These two observations call for additional comments. It should be first recalled that cobalt–hexammine complexes are indeed inert, but only kinetically since they are thermodynamically

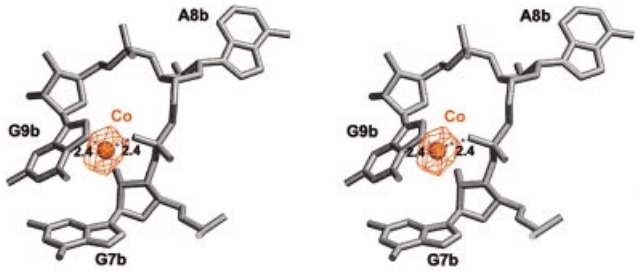

Figure 4. Anomalous difference map (contoured at 6.0 σ above mean level) showing inner-sphere binding of a cobalt tetrammine cation to N7 of a guanine and to the phosphate of a bulged-out adenine in the subtype-A DIS duplex. Distances between the cation and RNA ligands lie within 1.9–2.4 Å. This implies that two amines from the hexammine shell were displaced.

unstable (32). It has been shown that the exchange of the first ammine by a water molecule is by far the limiting kinetic step and proceeds through a pseudo first-order mechanism (36). The kinetic values from the latter study, obtained between 130 and 150°C, can be extrapolated at 37°C to yield an extremely small exchange rate constant of 2×10^{-11} s^{-1}. In addition, comparison of the absorption spectrum [in the conditions described in Martin and Swaddle (36)] of the $[Co(NH_3)]^{3+}$ solution that was used for crystal soaking (kept for 3 years under argon, in darkness and at 4°C) with the absorption spectrum of a freshly prepared solution did not reveal any detectable difference (not shown) and was fully comparable with the corresponding spectrum in Martin and Swaddle (36). Therefore, our observations cannot be explained by a significant dissociation of the hexammine compound during too long storage time prior to its use for soaking experiments. One may invoke some unknown reaction due to the presence of RNA, or of one chemical in the crystallization drops, or of both. Another hypothetical explanation would be that there was a radiolytic decomposition of cobalt hexammine catalyzed by a weak amount of Co^{2+} (36). However, in such a case, the binding of that species resulting from irradiation should have occurred in amorphous ice at 110 K. Even though we cannot reject a priori such a hypothesis in view of our recent findings on Br^- diffusion at the same temperature (37), other studies are clearly required to reconcile these conflicting results. Together, these data show that $[Mg(H_2O)_6]^{2+}$ substitution by a hexammine compound, which was indeed observed in other RNA crystal structures (33,34), may critically depend on unknown 'secondary' parameters.

Ba^{2+}, Ca^{2+} and Sr^{2+} are delocalized and induce a distortion of the helix

Calcium, strontium and barium, as magnesium, belong to the same group-2 alkaline earth metals. However, significant differences exist between Ca^{2+}, Sr^{2+} and Ba^{2+} in comparison with Mg^{2+}, essentially due to different ionic radii implying different coordination geometry (Table 2). This makes these ions less suitable than Co^{2+}, Mn^{2+} and Zn^{2+} for replacing Mg^{2+}. In the subtype-A DIS structure, after soaking of the crystals in Ca^{2+}, Sr^{2+} or Ba^{2+}-containing solutions, the three cations show similar binding properties to this duplex. First, they induce an identical significant lack of isomorphism compared with the 'native' Mg^{2+}-containing structure with a shortening by ~1.2 Å of the duplex length and, concomitantly, a significant

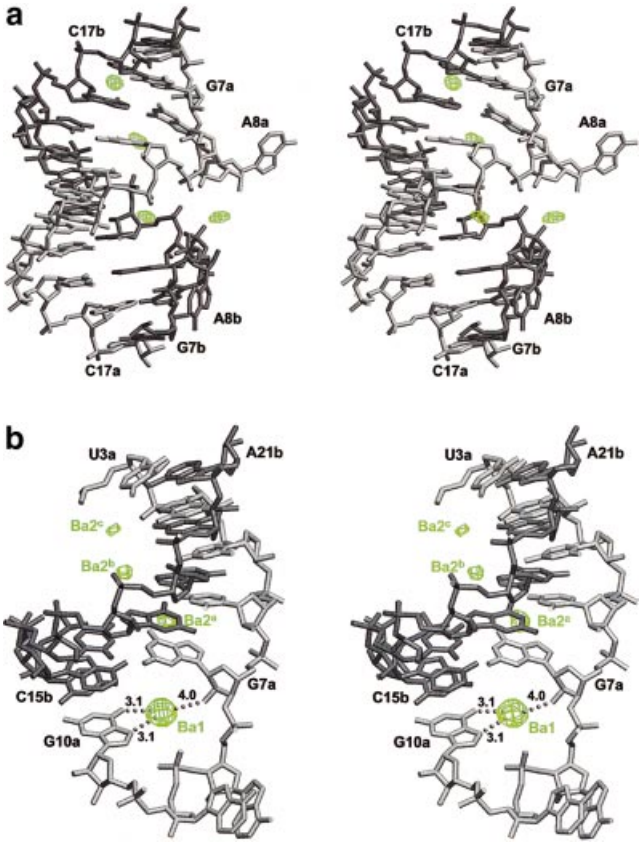

Figure 5. Loose binding of Ba^{2+} ions. (**a**) Poorly occupied binding sites for barium cations in the subtype-A DIS duplex. The anomalous difference map contoured at 4.5 σ above mean level is shown in green. (**b**) Ba^{2+} binding sites in the subtype-B DIS duplex. Three poorly occupied sites (depicted as $Ba2^a$, $Ba2^b$ and $Ba2^c$) lie in the major groove, whereas the Ba1 site is stronger and better localized in an internal bulge region. The anomalous difference map contoured at 6.0 σ above mean level is shown in green.

narrowing of the major groove. Secondly, these three cations display a clear preference for outer-sphere coordination to Hoogsteen sites of guanine residues in the major groove (Fig. 5a and b). Barium is the only tested divalent cation that did not bind at all at γ and γ' sites: instead Ba^{2+} bound to N7 and O6 atoms of both G7 and G9, as well as to the phosphate oxygen of A8 (Figs 2 and 5a). Thirdly, unlike Mg^{2+}, Mn^{2+}, Zn^{2+} and Co^{2+}, the binding sites for Ca^{2+}, Sr^{2+} and Ba^{2+} are much less localized. This is particularly true for Sr^{2+} since almost all guanine bases have a loosely bound strontium cation on their Hoogsteen site (Figs 2 and S2 in Supplementary Material). Accordingly, Ca^{2+}, Sr^{2+} and Ba^{2+} cations have higher temperature factors and lower occupancy values than their Mg^{2+} counterparts.

Among the three cations Ba^{2+}, Ca^{2+} and Sr^{2+}, only Ba^{2+} was used for soaking of a subtype-B DIS crystal. As for subtype-A DIS, Ba^{2+} binding sites are restricted to Hoogsteen sites of guanines, and they are rather weak and delocalized ($Ba2^a$, $Ba2^b$, $Ba2^c$; Fig. 5b) with one noticeable exception (Ba1; Fig. 5b). The latter is comparable with the site for Mn^{2+}, Co^{2+} and Zn^{2+} located in the internal loop formed around the bulged-out adenines A272, A273 (Fig. 3b). However, the

barium is more displaced toward the Hoogsteen sites O6 and N7 of G10 and interacts with them through inner-sphere coordination (Fig. 5b). Notably, the two sites related by non-crystallographic symmetry (G10a and G10b) are occupied by Ba^{2+} as this was the case for Co^{2+}, whereas only one site was occupied by Zn^{2+} and Mn^{2+}.

Other RNA crystal structures exhibit more ordered binding sites for Ca^{2+}, Sr^{2+} or Ba^{2+} after co-crystallization or crystal soaking. This is the case for the crystal structure of the hairpin ribozyme-inhibitor (38) and the U-rich bulge region of HIV-1 TAR RNA (39), where ordered octahedrally coordinated Ca^{2+} cations are found. Well ordered Sr^{2+} cations are found in the major groove and in the bulge region of the malachite green RNA aptamer (40), as well as in the acceptor arm of the $tRNA^{Ala}$ structure (41). In the latter structure the strontium cation is coordinated to nine ligands (among which four direct interactions with the RNA). About barium, a Ba^{2+} ion is found in the major groove of a small RNA duplex (42), bound to N7 and O6 atoms of a guanine and to four water molecules, but not in a classical octahedral geometry. Finally, Ba^{2+} ions were observed after crystal soaking in the structure of a lead-dependent ribozyme (43), either bound to the major groove to Hoogsteen sites of a guanine, via outer-sphere coordination, or directly bound to four atoms of the RNA, in a bulge region. But apart from the latter structure, all these binding sites result from co-crystallization of the RNA molecule with the metal ion, and not from crystal soaking as in the present study. It may be hypothesized that, in solution, an RNA molecule would adjust its structure to accommodate cations having binding geometries different from that of Mg^{2+} cations. By using crystal soaking, on the contrary, structural adjustments are likely to be more restricted by crystal packing and the binding of such cations might be disfavored.

Pb^{2+} and Cd^{2+} bind at dehydrated Mg^{2+} sites

Lead is known to induce cleavage at specific positions in RNA. As a result, Pb^{2+} is commonly used as a chemical probe for RNA structures. In particular, the kissing-loop complex formed by the subtype-A DIS is strongly cleaved in the presence of Pb^{2+} between A8 and G9 (44). It was therefore of particular interest to examine in detail Pb^{2+} binding to the duplex form of subtype-A DIS. Also interesting was the binding of cadmium since, on one hand, it can replace efficiently Mg^{2+} to induce cleavage in the hammerhead ribozyme (45) and, on the other hand, it inhibits cleavage of the hairpin ribozyme (46). Binding of these cations was probed by soaking of crystals of the subtype-A DIS duplex only. Magnesium was still present in the stabilizing solution (Table 1).

Both lead and cadmium strongly bind to γ and γ' Mg^{2+} sites by inner-sphere coordination, but with different affinities: Cd^{2+} preferably binds to site γ, whereas Pb^{2+} shows a marked preference for site γ' (Figs 2 and 6). Again, this illustrates that subtle differences can significantly affect cation binding since these two sites are a priori equivalent. No other magnesium site was replaced, possibly due to the competition with Mg^{2+} cations remaining in solution. To correlate the observed Pb^{2+} binding with cleavage in solution, lead probing on dissolved duplex crystals was performed. The resulting lead-induced cleavage pattern is different from that obtained for the kissing-loop complex, with a weak cleavage between G7 and A8, and a medium cleavage between A8 and G9 (not shown). Clearly, both cleavages can only occur after a minimal conformational change of the bulge region (especially for sugar pucker of the cleaved residues) to reach an adequate geometry needed for hydrolysis. This was also the case for $tRNA^{Phe}$ (47) and for the lead-dependent ribozyme (43). About cadmium, our results are in agreement with a protein–RNA complex showing several Cd^{2+} cations mostly interacting with the RNA by inner-sphere contacts on N7 atoms of purines and phosphate oxygens (48).

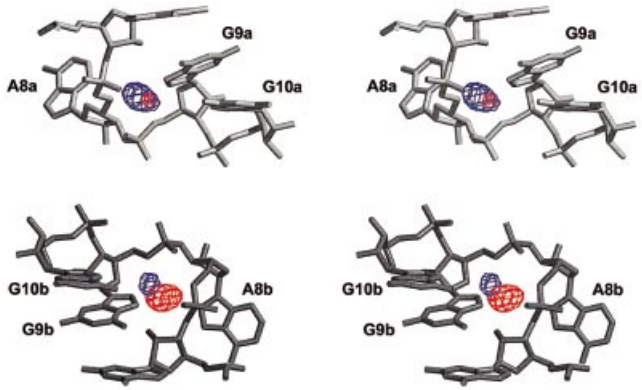

Figure 6. Binding of Pb^{2+} and Cd^{2+} to the subtype-A DIS duplex around bulged adenines A8a and A8b. The (Fo-Fc) difference map contoured at 6.0 σ for lead, and the anomalous difference map contoured at 5.0 σ above mean level for cadmium, are shown in blue and red, respectively.

Monovalent K^+ cations

Monovalent cations are known to be involved in charge neutralization required for RNA folding. Besides this non-specific role, monovalent cations, and potassium in particular, are implicated in more specific binding and long-range RNA recognition, as in the AA platform within the GAAA tetraloop receptor (19) or the ribosomal protein L11 RNA-binding site (49). Unlike divalent cations, monovalent cations usually require high-resolution data for an unambiguous identification in crystal structures. This is essentially due to their non-regular geometry, partially occupied binding sites and a cation-ligand distance close to typical values for water (Table 2). Furthermore, X-ray scattering of Na^+ is not so different from scattering of oxygen. As a consequence, Na^+ cations may be incorrectly assigned as water molecules unless the structure is solved at high resolution [see Tereshko *et al.* (20) for an excellent review about this topic].

Na^+ and K^+ were present in crystallization conditions of both subtype-A and -B DIS duplexes. No obvious monovalent binding site could be found in the subtype-A DIS duplex, even in the 1.85 Å resolution zinc-bound structure. In the subtype-B DIS structure, on the contrary, three strong density peaks were identified as potassium cations due to cation-ligand distances in the range 2.8–3.0 Å, which excludes sodium and magnesium (also present in solution) having bonding distances of 2.4 and 2.1 Å, respectively (50). Furthermore, since the anomalous signal of potassium is 7 to 10 times higher than for magnesium and sodium at the wavelength used for data collection ($f'' = 0.42\ e^-$ for potassium, but only 0.04 and 0.06 e^- for sodium and magnesium at $\lambda = 0.93$ Å), the nature of these

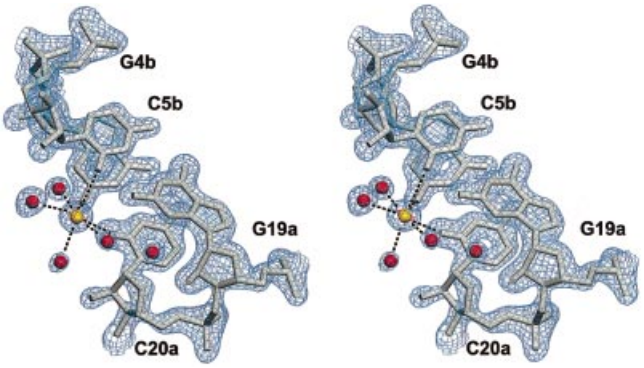

Figure 7. Potassium binding sites in the subtype-B DIS duplex. The (2Fo-Fc) electron density map contoured at 1.4 σ, and the anomalous difference maps contoured at 4.0 σ above mean level are shown in blue and red, respectively. Potassium ions and water molecules are represented as yellow and red spheres, respectively.

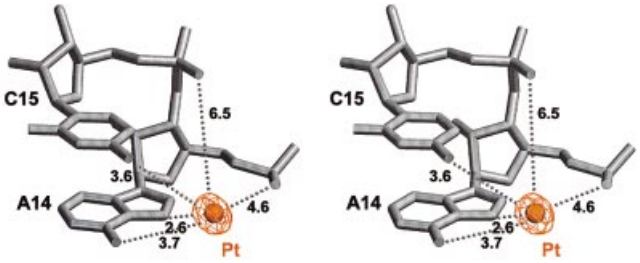

Figure 8. Pt^{4+} binding to 5′-AC-3′ sequences (here in the subtype-A DIS duplex). The anomalous difference map contoured at 10 σ above mean level is shown in orange.

cations could be confirmed by anomalous difference map whose highest peaks perfectly matched the three potential potassium sites. One binding site is located in the major groove, the cation being bound to carbonyl oxygens of the adjacent U6a-G18b and G7a-C17b base pairs (Fig. 2), as already observed in a previous RNA crystal structure (51). The two others are localized in the minor groove of the stems at G-C base pairs (Figs 2, 7 and S3 in Supplementary Material). In the case of Figure 7, the binding takes place on the two consecutive G-C and C-G base pairs of the G19aC20a and G4bC5b steps, whereas in the case of Figure S3 the binding is significantly displaced from the position related by non-crystallographic symmetry being stabilized by hydrogen bonds with a symmetry-related duplex. Notably, the K^+ binding site illustrated by Figure 7 (seen only in the subtype-B duplex) is the 'minor-groove equivalent' of the Mg^{2+} binding site α (seen only in the subtype-A duplex, Fig. 1b). It may thus be that K^+ and Mg^{2+} are mutually exclusive at, respectively, the minor-groove and major-groove sides of two consecutive G-C and C-G base pairs.

Replacement of Na^+ and K^+ by Rb^+, Cs^+ or Tl^+, which are easier to detect in electron density maps due to their larger *Z*-value and anomalous scattering properties, has been proposed for identification of monovalent ions in RNA crystal structures (19,20). In our case, however, Rb^+ was unable to bind to bona fide K^+ sites in the subtype-B DIS structure. Again, as for replacement of hexahydrated Mg^{2+} by cobalt hexammine, this points to the danger of drawing wrong conclusions when using such procedure in crystallographic studies. Finally, soaking of a subtype-A DIS crystal with Cs^+ did not reveal any site for this cation.

Pt^{4+} binds to 5′-AC-3′ sequences

Several X-ray structures of Pt(II)-nucleic acid complexes are known, especially concerning *cis*-diamminedichloroplatinium(II) (cisplatin) which is a well-known anticancer agent. Contrary to Pt(II), which can adopt square-planar and octahedral geometry, Pt(IV) adopts only an octahedral geometry. In this study, a $PtCl_4$ salt was used, originally as a heavy atom for structure solution. For that goal, subtype-A and -B DIS duplex crystals were soaked in solutions containing 5 mM $MgCl_2$ and 1 mM $PtCl_4$ (higher concentrations of $PtCl_4$ induced crystal cracking). Two Pt^{4+} cations were localized by anomalous difference maps in the subtype-A DIS. Despite incompleteness of the data (Table 1), one site was found in the subtype-B DIS. In all cases, the Pt^{4+} cation was bound to 5′-ApC-3′ sequences of the duplex (Figs 2 and 8), interacting with atoms N7 (2.6–3.0 Å), N6 (3.7–4.0 Å), the phosphate oxygen (4.3–4.6 Å) of the adenine, and N4 of the cytosine (3.6–4.2 Å). In agreement with the anomalous signal that dramatically decreased with resolution, the cation temperature factors were rather high (~75 $Å^2$), indicating a delocalized binding. This is rather surprising in view of the numerous anchoring points of the cation to the RNA. Notably, an identical Pt(IV) binding on two 5′-ApC-3′ steps in the $tRNA^{Phe}$ was already observed after soaking of crystals in K_2PtCl_6 (52). Therefore, due to its specificity towards 5′-ApC-3′ sequences implying a lack of competition with Mg^{2+} cations, and due to its anomalous scattering properties, Pt^{4+} is a possible candidate as a heavy atom/anomalous scatterer for RNA structure determination

Au^{3+} binds within WC sites of an accessible G-C base pair

Ruthenium hexammine and Au^{3+} cations were used to solve the structure of the subtype-B DIS duplex. One crystal was soaked overnight in a reservoir solution containing 10 mM $AuCl_3$ and data were collected at the absorption peak wavelength in order to maximize the anomalous signal for this metal. The obtained structure revealed two binding sites related by 2-fold non-crystallographic symmetry, at particularly unexpected positions: the Au^{3+} cation induced a deprotonation of N1 of the G7 residues and bound within the Watson–Crick sites of the two G7-C17 base pairs of the duplex (Figs 2 and 9). These two base pairs are particularly accessible to solvent due the presence of a cavity formed by unpaired adenines A8, A9 and A16 (Figs 1a and 9a). Notably, the last G1-C23 base pair is not accessible to solvent due to crystal packing involving pseudo-infinite helices and, accordingly, did not bind gold cations. The binding of Au^{3+} certainly perturbed the G7-C17 base pair, but did not disrupt it (Fig. 9b and c). The cation is coordinated following a (distorted) square-planar geometry in agreement with the usual behavior of cations like Rh(I), Ir(I), Ni(II), Pd(II), Pt(II) and Au(III) having an electronic configuration d^8 (32). Here, Au^{3+} is bound to N3 of C17 (2.2 Å), O2 of C17 (2.8 Å), N2 of G7 (2.1 Å), and to the deprotonated N1 of G7 (1.9 Å). Thus, such Au^{3+}

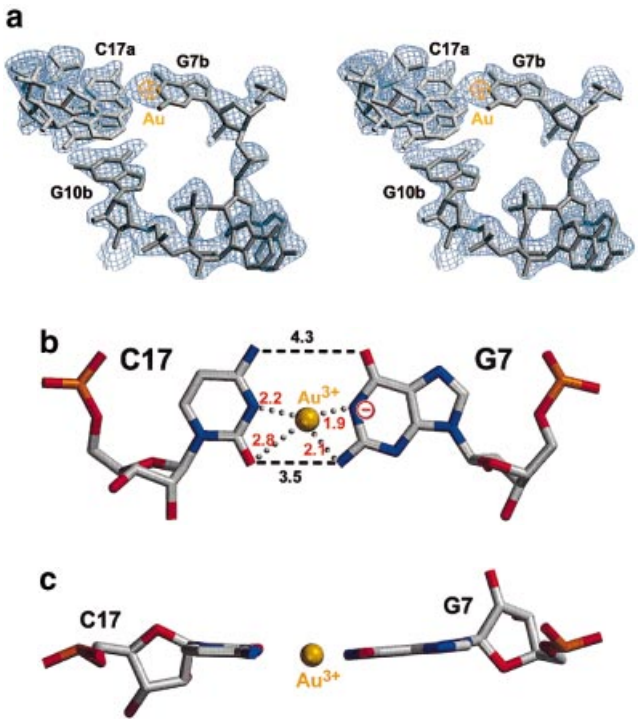

Figure 9. Au^{3+} binding to the accessible G7-C17 base pair of the subtype-B DIS duplex. (**a**) Stereoview showing the accessibility of the G7b-C17a pair bound to a gold cation. The composite simulated annealing omit map contoured at 1.3 σ is shown in blue and the anomalous difference map contoured at 13.0 σ above mean level in orange. (**b** and **c**) Schematic drawing showing interactions occurring between the cytosine, the gold(III) and the deprotonated guanine.

binding should be disfavored at acidic pH. Very likely, the two hydrogen atoms of the N2 amino group are pushed away perpendicularly to the plane of the base pair. It should be mentioned that the occupancy for the gold cation was refined to ~40%. It is not known whether this is due to thermodynamic or kinetic limitation. Note also that the accuracy of the four cation-ligand distances probably suffers from the resulting electron density map showing an apparent superposition of perturbed and unpertubed G-C base pairs.

This kind of binding between Au^{3+} and a G-C base pair resembles the one occurring between Hg^{2+} a T-T non-canonical base pair (53). In such complexes, the mercury induces a deprotonation of N3 of each thymine, which yields a highly stable complex (54). To our knowledge, the present structure represents the first nucleic acid structure in complex with Au(III) and also the first structure with such a cation-mediated G-C base pair. It would be certainly of interest to investigate the stability of this G–Au(III)–C interaction. If it turned out to be stable enough, Au^{3+} might possibly be used as a chemical probe for such accessible G-C base pairs. Since this cation does not inhibit the reverse transcriptase (55) this could be achieved by detecting an Au^{3+}-dependent strong stop on a cDNA. Finally, Au^{3+} cation did not bind to the subtype-A DIS duplex, in agreement with the absence of accessible G-C pair in this structure.

CONCLUSION

In spite of the rather small size of our model RNA structures, many conclusions can be drawn about metal ion binding to RNA from the present work, which probably represents the most comprehensive study of that kind. First, it emerges that all tested divalent cations have a marked preference for binding Hoogsteen sites of guanines, as reported previously for Mg^{2+} (30). Among them, Mn^{2+}, Co^{2+} and Zn^{2+} are the best candidates for replacing Mg^{2+}. However, because these three cations are softer than Mg^{2+} (56), they have a preference for inner-sphere coordination (Fig. 2). These observations are confirmed by an analysis of divalent metal ions binding in the numerous RNA crystal structures that have been published so far, in particular in the $tRNA^{Phe}$ (57) and in the hammerhead ribozyme (58,59). This is not the case for Ca^{2+}, Sr^{2+} and Ba^{2+} cations, having larger ionic radii and adopting a cubic geometry (however, Ca^{2+} can also adopt an octahedral geometry, see Table 2). According to our results, the latter divalent ions bind loosely to RNA, resulting in low occupancy and high thermal motion factor. It may be that, apart for specifically structured non-helical regions, some rearrangement within the RNA might be required for their specific binding. Interestingly, this segregation between 'good binders' on one hand, that is Mn^{2+}, Co^{2+} and Zn^{2+}, and 'poorer binders' on the other hand, that is Ca^{2+}, Sr^{2+} and Ba^{2+}, is consistent with a ranking of divalent cations in the 'Irving-Williams series' ($Ba^{2+} < Sr^{2+} < Ca^{2+} < Mg^{2+} < Mn^{2+} < Fe^{2+} < Co^{2+} < Ni^{2+} < Cu^{2+} < Zn^{2+}$) for the stability of the complexes they form with various ligands (32).

Strikingly, the two tested hexammines did not efficiently replace hexahydrated magnesium cations. Furthermore, a tetrammine cobalt cation was observed directly coordinated to a phosphate and to N7 of a guanine after the loss of two ammines. No simple explanation could be given for such a contradiction with the commonly accepted belief that cobalt-hexammine is a good mimic of hexahydrated magnesium. Thus, in the absence of more data, one cannot exclude that solution experiments based only upon this supposed mimicry might yield erroneous results. Lead and cadmium were exclusively found interacting by inner-sphere contacts in the vicinity of bulged adenine residues. Unlike all multivalent cations, potassium was the only minor groove binder but was also observed in the major groove bound to a G-U mismatch. Finally, unlike divalent cations, Pt^{4+} and Au^{3+} did not bind at magnesium sites. Rather, Pt^{4+} displayed a clear sequence-specific binding for 5′-ApC-3′ steps in helices as already observed in tRNA(Phe), whereas Au^{3+} only bound to Watson–Crick sites of two accessible G-C base pairs after deprotonation of N1 of the G. Finally, it appeared in many instances that the binding of a given cation to apparently analogous sites was strikingly dependent on unclear parameters that could be related to significant differences in hydration, the latter being likely due to irrelevant differences in crystal packing. This probably makes it somewhat illusory to draw firm conclusions on the mode of binding of a given cation based upon a single crystallographic example.

SUPPLEMENTARY MATERIAL

Supplementary Material is available at NAR Online.

ACKNOWLEDGEMENTS

We are grateful to Bernard and Chantal Ehresmann for their constant support. We thank Philippe Carpentier (ESRF, BM30), Christoph Hermes and Ehmke Pohl (DESY, BW7A) for their assistance during data collection and Pascal Auffinger (CNRS UPR 9002) for fruitful discussions. This work has been supported by the 'Agence Nationale de Recherche sur le SIDA' (ANRS). E.E. is a recipient of a fellowship from the ANRS.

REFERENCES

1. Weinstein,L.B., Jones,B.C., Cosstick,R. and Cech,T.R. (1997) A second catalytic metal ion in group I ribozyme. *Nature*, **388**, 805–808.
2. Sood,V.D., Beattie,T.L. and Collins,R.A. (1998) Identification of phosphate groups involved in metal binding and tertiary interactions in the core of the Neurospora VS ribozyme. *J. Mol. Biol.*, **282**, 741–750.
3. Yoshida,A., Sun,S. and Piccirilli,J.A. (1999) A new metal ion interaction in the Tetrahymena ribozyme reaction revealed by double sulfur substitution. *Nature Struct. Biol.*, **6**, 318–321.
4. Kieft,J.S. and Tinoco,I.,Jr (1997) Solution structure of a metal-binding site in the major groove of RNA complexed with cobalt (III) hexammine. *Structure*, **5**, 713–721.
5. Colmenarejo,G. and Tinoco,I.,Jr (1999) Structure and thermodynamics of metal binding in the P5 helix of a group I intron ribozyme. *J. Mol. Biol.*, **290**, 119–135.
6. Gonzalez,R.L.,Jr and Tinoco,I.,Jr (1999) Solution structure and thermodynamics of a divalent metal ion binding site in an RNA pseudoknot. *J. Mol. Biol.*, **289**, 1267–1282.
7. Schmitz,M. and Tinoco,I.,Jr (2000) Solution structure and metal-ion binding of the P4 element from bacterial RNase P RNA. *RNA*, **6**, 1212–1225.
8. Rudisser,S. and Tinoco,I.,Jr (2000) Solution structure of Cobalt(III)hexammine complexed to the GAAA tetraloop and metal-ion binding to G·A mismatches. *J. Mol. Biol.*, **295**, 1211–1223.
9. Tanaka,Y., Kojima,C., Morita,E.H., Kasai,Y., Yamasaki,K., Ono,A., Kainosho,M. and Taira,K. (2002) Identification of the metal ion binding site on an RNA motif from hammerhead ribozymes using (15)N NMR spectroscopy. *J. Am. Chem. Soc.*, **124**, 4595–4601.
10. Pilbrow,J.R. and Hanson,G.R. (1993) Electron paramagnetic resonance. In Riordan,J.F. and Vallee,B.L. (eds), *Methods Enzymology*, Vol. 227, pp. 330–353.
11. Hermann,T. and Westhof,E. (1998) Exploration of metal ion binding sites in RNA folds by Brownian-dynamics simulations. *Structure*, **6**, 1303–1314.
12. Skripkin,E., Paillart,J.C., Marquet,R., Ehresmann,B. and Ehresmann,C. (1994) Identification of the primary site of the Human Immunodeficiency Virus Type I RNA dimerization *in vitro*. *Proc. Natl Acad. Sci. USA*, **91**, 4945–4949.
13. Muriaux,D., Rocquigny,H.D., Roques,B.P. and Paoletti,J. (1996) NCP7 activates HIV-1 Lai RNA dimerization by converting a transient loop–loop complex into a stable dimer. *J. Biol. Chem.*, **271**, 33686–33692.
14. Ennifar,E., Walter,P., Ehresmann,B., Ehresmann,C. and Dumas,P. (2001) Crystal structures of coaxially stacked kissing complexes of the HIV-1 RNA dimerization initiation site. *Nature Struct. Biol.*, **8**, 1064–1068.
15. Ennifar,E., Yusupov,M., Walter,P., Marquet,R., Ehresmann,B., Ehresmann,C. and Dumas,P. (1999) The crystal structure of the dimerization initiation site of genomic HIV-1 RNA reveals an extended duplex with two adenine bulges. *Structure*, **7**, 1439–1449.
16. Otwinowski,Z. and Minor,W. (1996) Processing of X-ray diffraction data collected in oscillation mode. In Carter,C.W.,Jr and Sweet,R.M. (eds), *Methods Enzymology.* Vol. 276, pp. 307–326.
17. Brünger,A.T., Adams,P.D., Clore,G.M., DeLano,W.L., Gros,P., Grosse-Kunstleve,R.W., Jiang,J.S., Kuszewski,J., Nilges,M., Pannu,N.S. *et al.* (1998) Crystallography and NMR system: A new software suite for macromolecular structure determination. *Acta Crystallogr.*, **D54**, 905–921.
18. Collaborative Computational Project Number 4. (1994) The CCP4 Suite: Programs for Protein Crystallography. *Acta Crystallogr.*, **D50**, 760–763.
19. Basu,S., Rambo,R.P., Strauss-Soukup,J., Cate,J.H., Ferré-D'Amaré,A.R., Strobel,S.A. and Doudna,J.A. (1998) A specific monovalent metal ion integral to the AA platform of the RNA tetraloop receptor. *Nature Struct. Biol.*, **5**, 986–992.
20. Tereshko,V., Wilds,C.J., Minasov,G., Prakash,T.P., Maier,M.A., Howard,A., Wawrzak,Z., Manoharan,M. and Egli,M. (2001) Detection of alkali metal ions in DNA crystals using state-of-the-art X-ray diffraction experiments. *Nucleic Acids Res.*, **29**, 1208–1215.
21. Ennifar,E., Walter,P. and Dumas,P. (2001) An efficient method for solving RNA structures: MAD phasing by replacing magnesium with zinc. *Acta Crystallogr.*, **D57**, 330–332.
22. Misra,V.K. and Draper,D.E. (1999) The interpretation of Mg^{2+} binding isotherms for nucleic acids using Poisson–Boltzmann theory. *J. Mol. Biol.*, **294**, 1135–1147.
23. Westhof,E. (1988) Water: an integral part of nucleic acid structure. *Ann. Rev. Biophys. Biophys. Chem.*, 125–144.
24. Auffinger,P. and Westhof,E. (2000) RNA solvation: a molecular dynamics simulation perspective. *Biopolymers*, **56**, 266–274.
25. Cate,J.H., Gooding,A.R., Podell,E., Zhou,K., Golden,B.L., Kundrot,C.E., Cech,T.R. and Doudna,J.A. (1996) Crystal structure of a group I ribozyme domain: principles of RNA packing. *Science*, **273**, 1678–1685.
26. Wimberly,B.T., Brodersen,D.E., Clemons,W.M.,Jr, Morgan-Warren,R.J., Carter,A.P., Vonrhein,C., Hartsch,T. and Ramakrishnan,V. (2000) Structure of the 30S ribosomal subunit. *Nature*, **407**, 327–339.
27. Cruse,W.B.T., Saludjan,P., Biala,E., Strazewski,P., Prangé,T. and Kennard,O. (1994) Structure of a mispaired RNA double helix at 1.6 Å resolution and implication for the prediction of RNA secondary structure. *Proc. Natl Acad. Sci. USA*, **91**, 4160–4164.
28. Cruse,W., Saludjian,P., Neuman,A. and Prangé,T. (2001) Destabilizing effect of a fluorouracil extra base in a hybrid RNA duplex compared with bromo and chloro analogues. *Acta Crystallogr.*, **D57**, 1609–1613.
29. Teplova,M., Minasov,G., Tereshko,V., Inamati,G.B., Cook,P.D., Manoharan,M. and Egli,M. (1999) Crystal structure and improved antisense properties of 2′-*O*-(2-methoxyethyl)-RNA. *Nature Struct. Biol.*, **6**, 535–539.
30. Robinson,H., Gao,Y., Sanishvili,R., Joachimiak,A. and Wang,A.H.-J. (2000) Hexahydrated magnesium ions bind in the deep major groove and at the outer mouth of A-form nucleic acid duplexes. *Nucleic Acids Res.*, **28**, 1760–1766.
31. Cowan,J.A. (1993) Metallobiochemistry of RNA. $[Co(NH_3)_6]^{3+}$ as a probe for Mg^{2+}(aq) binding sites. *J. Inorg. Biochem.*, **49**, 171–175.
32. Shriver,D.F. and Atkins,P.W. (1999) *Inorganic Chemistry*. Oxford University Press, Oxford.
33. Cate,J.H. and Doudna,J.A. (1996) Metal-binding sites in the major groove of a large ribozyme domain. *Structure*, **4**, 1221–1229.
34. Juneau,K., Podell,E., Harrington,D.J. and Cech,T.R. (2001) Structural basis of the enhanced stability of a mutant ribozyme domain and a detailed view of RNA-solvent interactions. *Structure*, **9**, 221–231.
35. Vargason,J.M., Eichman,B.F. and Ho,P.S. (2000) The extended and eccentric E-DNA structure induced by cytosine methylation or bromination. *Nature Struct. Biol.*, **7**, 758–761.
36. Martin,A. and Swaddle,T.W. (1974) Kinetics and mechanism of the thermal decomposition of hexaamminecobalt(III) and aquopentaamminecobalt(III) ions in acidic aqueous solutions. *Can. J. Chem.*, **52**, 2751–2759.
37. Ennifar,E., Carpentier,P., Pirocchi,M., Walter,P., Ferrer,J.L. and Dumas,P. (2002) X-ray-induced debromination of nucleic acids at the Br K-absorption edge and implications on MAD-phasing. *Acta Crystallogr.*, **D58**, 1262–1268.
38. Rupert,P.B. and Ferré-D'Amaré,A.R. (2001) Crystal structure of a hairpin ribozyme-inhibitor complex with implications for catalysis. *Nature*, **410**, 780–786.
39. Ippolito,J.A. and Steitz,T.A. (1998) A 1.3-Å resolution crystal structure of the HIV-1 *trans*-activation response region RNA stem reveals a metal ion-dependent bulge conformation. *Proc. Natl Acad. Sci. USA*, **95**, 9819–9824.
40. Baugh,C., Grate,D. and Wilson,C. (2000) 2.8 Å crystal structure of the malachite green aptamer. *J. Mol. Biol.*, **301**, 117–128.
41. Mueller,U., Schubel,H., Sprinzl,M. and Heinemann,U. (1999) Crystal structure of acceptor stem of tRNA(Ala) from *Escherichia coli* shows unique G·U wobble base pair at 1.16 Å resolution. *RNA*, **5**, 670–677.
42. Perbandt,M., Vallazza,M., Lippmann,C., Betzel,C. and Erdmann,V.A. (2001) Structure of an RNA duplex with an unusual G·C pair in wobble-like conformation at 1.6 Å resolution. *Acta Crystallogr.*, **D57**, 219–224.

43. Wedekind,J.E. and McKay,D.B. (1999) Crystal structure of a lead-dependent ribozyme revealing metal binding sites relevant to catalysis. *Nature Struct. Biol.*, **6**, 261–268.
44. Paillart,J.C., Westhof,E., Ehresmann,C., Ehresmann,B. and Marquet,R. (1997) Non-canonical interactions in a kissing loop complex: the dimerization initiation site of HIV-1 genomic RNA. *J. Mol. Biol.*, **270**, 36–49.
45. Dahm,S.C., Derrick,W.B. and Uhlenbeck,O.C. (1993) Evidence for the role of solvated metal hydroxide in the hammerhead cleavage mechanism. *Biochemistry*, **32**, 13040–13045.
46. Walter,F., Murchie,A.I., Thomson,J.B. and Lilley,D.M. (1998) Structure and activity of the hairpin ribozyme in its natural junction conformation: effect of metal ions. *Biochemistry*, **37**, 14195–14203.
47. Brown,R.S., Hingerty,B.E., Dewan,J.C. and Klug,A. (1983) Pb(II)-catalysed cleavage of the sugar-phosphate backbone of yeast tRNAPhe—implications for lead toxicity and self-splicing RNA. *Nature*, **303**, 543–546.
48. Wimberly,B.T., Guymon,R., McCutcheon,J.P., White,S.W. and Ramakrishnan,V. (1999) A detailed view of a ribosomal active site: the structure of the L11-RNA complex. *Cell*, **97**, 491–502.
49. Conn,G.L., Gittis,A.G., Lattman,E.E., Misra,V.K. and Draper,D.E. (2002) A compact RNA tertiary structure contains a buried backbone-K+ complex. *J. Mol. Biol.*, **318**, 963–973.
50. Marcus,Y. (1988) Ionic radii in aqueous solutions. *Chem. Rev.*, **88**, 1475–1498.
51. Batey,R.T., Rambo,R.P., Lucast,L., Rha,B. and Doudna,J.A. (2000) Crystal structure of the ribonucleoprotein core of the signal recognition particle. *Science*, **287**, 1232–1239.
52. Kim,S.H., Shin,W.C. and Warrant,R.W. (1985) Heavy metal ion-nucleic acid interaction. *Methods Enzymol.*, **114**, 156–167.
53. Kosturko,L.D., Folzer,C. and Stewart,R.F. (1974) The crystal and molecular structure of a 2:1 complex of 1-methylthymine-mercury (II). *Biochemistry*, **13**, 3949–3952.
54. Katz,S. (1963) The reversible reaction of Hg(II) and double-stranded polynucleotides. A step-function theory and its significance. *Biochim. Biophys. Acta*, **68**, 240–253.
55. Sabbioni,E., Blanch,N., Baricevic,K. and Serra,M.A. (1999) Effects of trace metal compounds on HIV-1 reverse transcriptase: an *in vitro* study. *Biol. Trace Elem. Res.*, **68**, 107–119.
56. Pearson,R.G. (1963) Hard and soft acids and bases. *J. Am. Chem. Soc.*, **85**, 3533–3539.
57. Jack,A., Ladner,J.E., Rhodes,D., Brown,R.S. and Klug,A. (1977) A crystallographic study of metal-binding to yeast phenylalanine transfer RNA. *J. Mol. Biol.*, **111**, 315–328.
58. Scott,W.G., Murray,J.B., Arnold,J.R.P., Stoddard,B.L. and Klug,A. (1996) Capturing the structure of a catalytic RNA intermediate: the hammerhead ribozyme. *Science*, **274**, 2065–2069.
59. Murray,J.B., Terwey,D.P., Maloney,L., Karpeisky,A., Usman,N., Beigelman,L. and Scott,W.G. (1998) The structural basis of hammerhead ribozyme self-cleavage. *Cell*, **92**, 665–673.